Tutorial: An introduction to terahertz time domain spectroscopy (THz-TDS)

Jens Neu, and Charles A. Schmuttenmaer

Citation: Journal of Applied Physics **124**, 231101 (2018); doi: 10.1063/1.5047659
View online: https://doi.org/10.1063/1.5047659
View Table of Contents: http://aip.scitation.org/toc/jap/124/23
Published by the American Institute of Physics

JOURNAL OF APPLIED PHYSICS **124**, 231101 (2018)

Tutorial: An introduction to terahertz time domain spectroscopy (THz-TDS)

Jens Neu[a] and Charles A. Schmuttenmaer[b]
Department of Chemistry, Yale University, New Haven, Connecticut 06520-8107, USA

(Received 9 July 2018; accepted 24 November 2018; published online 17 December 2018)

Terahertz time-domain spectroscopy (THz-TDS) is a powerful technique for material's characterization and process control. It has been used for contact-free conductivity measurements of metals, semiconductors, 2D materials, and superconductors. Furthermore, THz-TDS has been used to identify chemical components such as amino acids, peptides, pharmaceuticals, and explosives, which makes it particularly valuable for fundamental science, security, and medical applications. This tutorial is intended for a reader completely new to the field of THz-TDS and presents a basic understanding of THz-TDS. Hundreds of articles and many books can be consulted after reading this tutorial. We explore the basic concepts of TDS and discuss the relationship between temporal and frequency domain information. We illustrate how THz radiation can be generated and detected, and we discuss common noise sources and limitations for THz-TDS. This tutorial concludes by discussing some common experimental scenarios and explains how THz-TDS measurements can be used to identify materials, determine complex refractive indices (phase delay and absorption), and extract conductivity. *Published by AIP Publishing.* https://doi.org/10.1063/1.5047659

I. INTRODUCTION

Terahertz time-domain spectroscopy (THz-TDS) has become a valuable technique in the fields of chemistry,[1] materials sciences,[2] engineering,[3] and medicine.[4–6] The range of applications is so large[7–9] that we could focus only on a few examples after introducing the basics.

The spectral range between 0.1 THz and 10 THz ($3.3\,cm^{-1}$–$333\,cm^{-1}$) is an important region for low frequency dielectric relaxation and vibrational spectroscopy of liquids, such as water, methanol, ethanol, propanol, and others.[10,11] It has also been particularly important in the study of low frequency modes in molecular crystals. THz-TDS in combination with density functional theory (DFT)[12–18] can be used to study amino acids,[14,18–23] peptides,[24–26] drugs,[27] and explosives.[17,28,29] The latter two are particularly interesting due to the ability of THz radiation to penetrate through clothing[30] and packaging.[31] There are also applications where THz-TDS is being optimized for the detection of bombs, drugs, and weapons.[32,33]

In the field of materials science, THz-TDS is ideally suited to measure mobile charge carriers since they reflect and absorb THz radiation. THz-TDS has been used to measure conductivity,[34] topological insulators (TI),[35,36] and superconductors,[37,38] as well as phase transitions in these materials.[39] Furthermore, 2D materials like bismuth selenide (Bi_2Se_3)[40] and graphene[41,42] have been studied. In the case of graphene, spatially resolved THz-TDS has been demonstrated as an effective tool to validate the homogeneity and uniformity of fabricated layers.[43] In addition, the interest in THz-TDS as a quality control technique is growing. For example, THz-TDS can be used to measure the drying process and final thickness of paint coatings, reducing costs and process times.[44–46]

The interest in THz-TDS from the medical community has been growing in recent years. Proof-of-concept experiments are able to detect skin cancer[47] and to monitor scar growth.[48] Furthermore, THz-TDS can also be used to detect yeast,[49] bacteria,[49,50] and viruses[51] via THz-metamaterials.

Metamaterials comprise human-made, sub-wavelength structures. The local field enhancement in these structures significantly increases the sensitivity of THz-TDS and therefore allows the measurement of extremely small concentrations and new commercial applications.[52,53] THz wavelengths are on the order of $300\,\mu m$, so achieving the sub-wavelength criterion is easily attainable with current lithographic techniques. In addition, the lack of classical optical components in this frequency range sparked the research of THz metamaterials. Metamaterial based filter (static[54,55] and dynamic[56]) lenses,[57,58] beamsteerers,[59,60] and *perfect* absorbers[61] have been characterized with THz-TDS.

The wide variety of applications has resulted in quite a number of different configurations of THz spectrometers.[62–64] We focus on general considerations and provide explanations and illustrations to provide an overview of the field of THz-TDS. That is, we explain THz-TDS in a general sense and how time domain measurements can provide spectral information. We also illustrate the method for extracting optical properties from the measured signal, as well as some potential pitfalls when acquiring THz-TDS spectra.

We first discuss the basic concepts of THz-TDS in Sec. II. In Sec. III, we present several techniques to generate coherent THz radiation, and in Sec. IV, we present how to detect THz. These sections are focused on photoconductive antennas, the most common THz-TDS emitter/detector. We define some figure-of-merit benchmarks for a THz-TDS system and discuss some common noise sources, which provide a starting point for the optimization of an existing system (Sec. V). We conclude this tutorial with a short overview of THz-TDS experiments related to materials science and spectroscopy in Sec. VI.

---

[a] Electronic mail: jens.neu@yale.edu
[b] Electronic mail: charles.schmuttenmaer@yale.edu

0021-8979/2018/124(23)/231101/14/$30.00

II. CONCEPT OF TIME-DOMAIN SPECTROSCOPY (TDS)

Spectroscopy refers to the energy, wavelength, or frequency of photons that pass through a sample. In the case of THz-TDS, the time-domain signal directly measures the transient electric field rather than its intensity.

The THz electric field at the detector is typically on the order of 10–100 V/cm[65] and has a time duration of a few picoseconds. Therefore, a fast and sensitive detection method of the electric field is required. Direct electrical detectors and circuits usually have rise times and fall times in the picosecond to nanosecond range and, therefore, do not have high enough time resolution. The way to reach sub-picosecond resolution is by using optical techniques wherein an ultrashort NIR optical pulse (typically shorter than 100 fs) is beamsplit along two paths to generate and detect the time-dependent THz field, as discussed below.

Measuring in the time-domain is based on sampling the unknown THz field with a known femtosecond laser pulse, which is referred to as the *read-out pulse*. THz-TDS uses the convolution of a short read-out pulse with the longer THz pulse. Several different methods can be used to perform this convolution, which are briefly discussed in Sec. IV. All of these detectors have two things in common: they measure the THz field rather than intensity and a signal is obtained only when the optical read-out pulse arrives simultaneously with the THz pulse. Without discussing the details of the detection mechanism, we can describe the signal, $S(t)$, as

$$S(t) \propto I_{opt}(t)E_{\mathrm{THz}}(t), \tag{1}$$

with $I_{opt}(t)$ being the intensity profile of the laser pulse and $E_{\mathrm{THz}}(t)$, the electrical field of the THz pulse at time t. This is the instantaneous signal that must be detected with sub-picosecond resolution. All existing detectors are too slow, so the convolution ($\circledast$) of the two pulses is measured instead

$$S(t_1) \propto I_{opt}(t) \circledast E_{\mathrm{THz}}(t_1). \tag{2}$$

Since the optical pulse is significantly shorter than the THz pulse, it can be approximated as a delta-function

$$S(t_1) \propto I_{opt}(t) \circledast E_{\mathrm{THz}}(t_1) \approx \delta(t) \circledast E_{\mathrm{THz}}(t_1) = E_{\mathrm{THz}}(t_1). \tag{3}$$

The fact that the detector is only sensitive if both pulses arrive simultaneously and that the optical pulse is significantly shorter than the THz pulse allows us to measure the THz field as a function of time. Furthermore, the detector is sensitive to the sign of the electrical field. That is, we measure the time-dependent amplitude $E(t)$, in contrast to other techniques such as FTIR which measure only the intensity $[E^2(t)]$ of an electromagnetic signal and, therefore, do not capture the phase information.

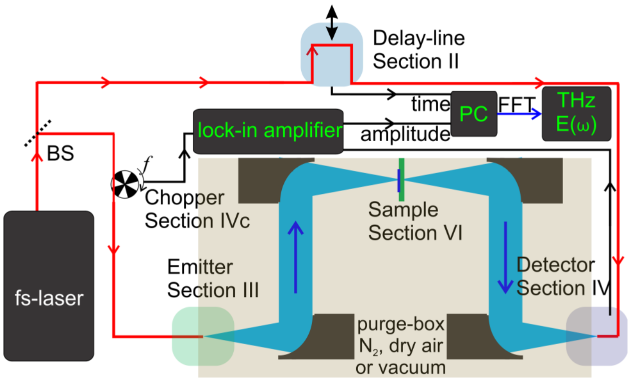

FIG. 1. Simplified THz time-domain spectrometer (THz-TDS). The output of a femtosecond laser pulse is split into two beams using a beamsplitter (BS). One beam is used to generate THz radiation, modulated with frequency f. The other beam is routed through a delay line and used to detect the THz beam. The black lines illustrate signal connections, inputting the modulation frequency and detected signal to a lock-in amplifier and a computer (PC). The individual components of this system are discussed in detail in the corresponding Secs. II–VI.

The measured signal corresponds to the THz field amplitude at a single point in time (t_1). The next step is to measure the signal at all time-points. This is achieved by delaying the read-out pulse relative to the THz pulse using a mechanical delay line. The output of the laser is split into two beams, as sketched in Fig. 1. One of the beams is used to generate THz radiation, and the other one is the read-out beam that detects it. The temporal delay is achieved by increasing the path length of one of the beams. The travel time of a laser pulse is $t = s/c$, where s is the path length and c is the speed of light (this corresponds to 30 cm/ns or 300 μm/ps). This simplifies the problem of femtosecond time resolution to one of micrometer spatial resolution. Precise micro positioning is achieved with computer-controlled positioning stages. In THz-TDS (and ultrafast spectroscopy in general), these stages are usually referred to as delay lines. The round trip delay time changes 6.6 fs for each micrometer of delay line displacement. The moving speed of the delay line defines the sampling speed in the time domain. It is, therefore, common to state the speed of the delay line in ps/s.

Water vapor has strong absorption features in the THz range that can interfere with measurements.[66,67] To minimize this absorption, the THz beam path is enclosed in a purge box (see Fig. 1) which is purged with dry air or nitrogen. Alternatively, the box can also be evacuated, but that requires a significantly higher level of design engineering.

The system sketched in Fig. 1 uses THz-TDS transmission geometry, which is the simplest one. However, it is also possible to measure the THz pulse reflected from the sample[68,69] or to use an attenuated total reflection geometry.[70] In addition, THz-TDS can also be used for the near-field detection of a sample.[57,71,72]

A. Fourier transformation

The measured THz transient electric field is Fourier transformed to yield the spectral information of the THz pulse. The Fourier transform of a real-valued time-domain pulse is a complex-valued frequency-domain spectrum, defined by[73]

$$\underbrace{E(t)}_{\mathbb{R}} \xrightarrow{\mathrm{FT}} \frac{1}{\sqrt{2\pi}}\int_{-\infty}^{\infty} E(t)\mathrm{e}^{-\mathrm{i}\omega t}\mathrm{d}t = \underbrace{E(\omega)}_{\mathbb{C}}. \tag{4}$$

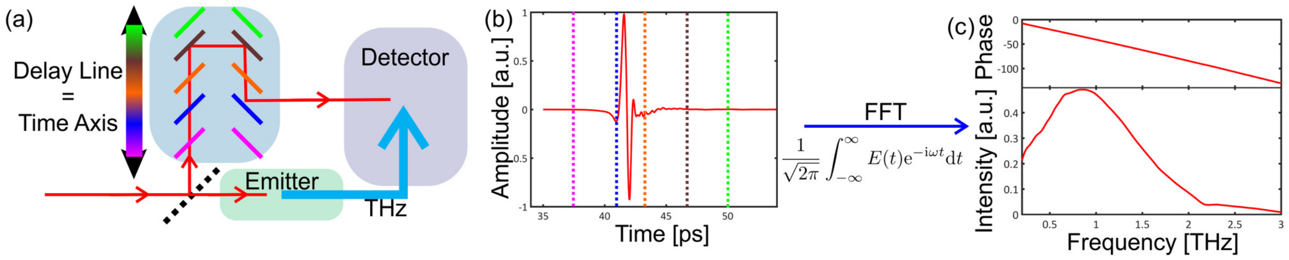

FIG. 2. (a) Simplified illustration of TDS. The different colors correspond to different delay-line positions. These positions correspond to different time points in (b). (b) Measured THz time-domain signal. (c) Fast Fourier transformation (FFT) of the signal in the frequency domain. The upper panel shows the unwrapped phase of the complex Fourier transform and the lower shows the amplitude.

The normalization factor, $(\frac{1}{\sqrt{2\pi}})$, as well as the sign in the exponential function are defined differently in different fields of study and the algorithm used, so care must be taken. For discretized experimental data, the Fourier transformation is replaced by a discrete Fourier transformation (DFT, or FFT if the fast Fourier transform algorithm is used).[74,75] Figure 2 shows a measured THz time trace and the resulting complex FFT in the frequency domain. The complex spectrum is separated into phase $[\phi(\omega)]$ and amplitude $[A(\omega)]$

$$E(\omega) = A(\omega)\mathrm{e}^{\mathrm{i}\phi(\omega)}. \tag{5}$$

The fact that the measurement yields amplitude and phase information is a significant advantage of THz-TDS compared to broadband infrared, single wavelength continuous-wave (CW) THz measurements, and visible spectroscopy. Measuring the spectra in this manner allows one to directly calculate the complex-valued refractive index $n(\omega)$, without needing to use the Kramers-Kronig relation.[76] These calculations are described in Sec. VI.

III. THz GENERATION

The heart of any THz-TDS system is an ultrafast laser oscillator or amplifier. This laser emits optical pulses with femtosecond pulse durations which are transformed into a picosecond THz pulse. This is achieved by the THz emitter. There exists a large variety of THz emitters currently in use. We present a short overview of the most important emitters bearing in mind that the most appropriate emitter design for a particular application is not always trivial to identify. Therefore, in this overview, we focus on two figures-of-merit: the achievable THz-bandwidth and the suitability to different laser systems.

A. Overview on THz emitters

The different emitters, summarized in Table I, can be categorized in two different groups based on the underlying mechanism for THz generation. One way to generate THz radiation is to induce a short current pulse in a medium, which then emits THz radiation as described in detail below. The other commonly used method is via a nonlinear optical rectification process which is primarily used in amplifier based systems.

For the user, the most important concern is typically whether an emitter can be used with an existing laser system. To allow a rough estimation, we labeled the different mechanisms with either oscillator (Osci.) or amplifier (amp). For the purpose of this tutorial, a laser oscillator has a repetition rate between 40 MHz and 1 GHz, a pulse length of less than 150 fs, and a pulse energy below 10 nJ. In contrast, the amplifier has a repetition rate of 1-10 kHz, with a pulse energy of more than 10 μJ and also a pulse length of less than 150 fs. Emitters and detectors typically increase in bandwidth and efficiency with shorter laser pulses.

The short overview in Table I should help the reader navigate the large realm of THz emitters, but this list is not exhaustive. The actual bandwidth and performance of the emitter will depend on the experimental conditions. Here, we will focus solely on THz generation from photoconductive antennas (PCAs).

B. THz generation from a PCA

When an electron changes its velocity (i.e., is accelerated), electromagnetic radiation is emitted.[76] This concept is used in a wide variety of experiments, for example, in

TABLE I. Overview of several THz generation techniques. The acronyms are: OR, optical rectification; TPFP, tilted pulse front pumping, subcategories of OR, and DAST (4-dimethylamino-N-methylstilbazolium tosylate); PCA, photoconductive antenna; SI-GaAs, semi-insulating gallium arsenide; r-SOS, radiation damaged silicon-on-sapphire; LT-GaAs, low temperature grown gallium arsenide.

Emitter name	Laser	Bandwidth (THz)	Reference
OR			77
LiNbO$_3$	Amplifier	0.1–3	78
ZnTe(110)	Amplifier	0.1–3	79
DAST	Amp/Osci.	0.1–180	80–82
TPFP	Amplifier	0.1–3.5	83–85
Air plasma	Amplifier	1–120	86–88
Photo-Dember	Amp/Osci.		89
InGaAs		0.1–6	90
InAs		0.1–2.5	91
Spintronic			
W/CoFeB/Pt	Amplifier	0.1–30	92
Fe/Pt	Oscillator	0.1–6	93
PCA	Oscillator		94,95
SI-GaAs		0.1–6	96 and 97
r-SOS		0.1–2	98 and 99
LT-GaAs		0.1–8 9–15	96 and 100
LT-GaAs,bonding		0.1–10	101–103

generating synchrotron radiation or X-ray bremsstrahlung. The formal reason for this effect can be derived from Maxwell's equations.[76] For the simple case of a dipole emitter that is much smaller than the wavelength being emitted having a diameter of w_0, the THz field observed at a distance r and angle α is given by[64]

$$E_{\mathrm{THz}}(t) \propto w_0 \frac{\sin(\alpha)}{r} \frac{\mathrm{d}|I_{PC}(t_r)|}{\mathrm{d}t_r}, \tag{6}$$

with t_r being the retarded time $t_r = t - r/c$, and $I_{PC}(t)$ is the photocurrent. A change in current results in an emitted electromagnetic field. If this current change occurs on a femtosecond timescale, the resulting emitted field has picosecond duration with concomitant THz bandwidth.

In a PCA, this current pulse is generated in between two metal contacts. These contacts are lithographically fabricated on a semiconductor and biased with a DC voltage (U_{DC}). The semiconductor is undoped and, therefore, has high resistivity and no current flows through the gap between the two metal contacts (with moderate bias voltages). As a result, the contacts act as a capacitor C. The energy W stored in a capacitor is

$$W(t) = \frac{1}{2} C U_{DC}^2(t). \tag{7}$$

The femtosecond laser pulse is focused on the gap between the metal contacts, as illustrated in Fig. 3. The photon energy of the pulse must be larger than the bandgap energy of the semiconductor. Consequently, the laser pulse excites electrons into the conduction band, which increases the conductivity of the semiconductor (and, therefore, reduces its resistivity). The bias voltage in conjunction with the photoinduced decrease in resistance creates a rapid current flow between the metal contacts, with a sharp rising edge determined by the temporal length of the laser pulse.

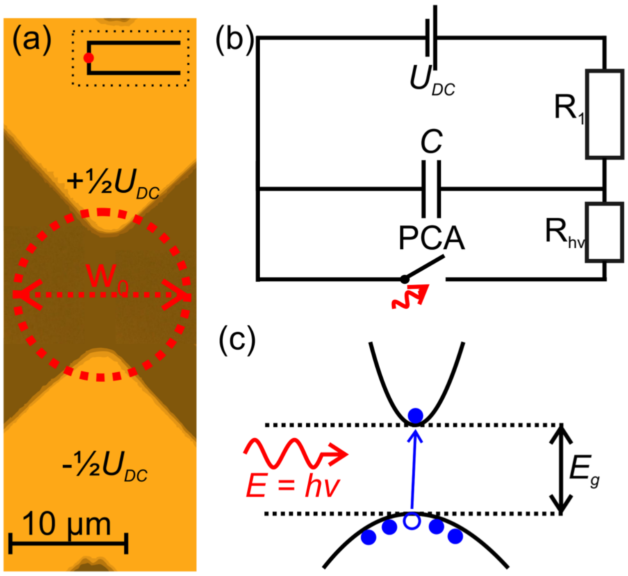

FIG. 3. (a) Optical microscope image of a dipole photoconductive antenna (PCA). The laser spot is focused in the gap, while a bias voltage is applied between the metallic contacts. Inset: overview of a simplified antenna, the red dashed circle indicates the location of the laser illumination. (b) Simplified electrical circuit diagram illustrating the basic concept of the photoconductive switch. (c) Simplified band scheme illustrating the photoexcitation by an photon with $E = h\nu > E_g$, i.e., larger than the bandgap.

The net current is limited by the charge and energy stored in the capacitor. As soon as the charges in the gap are accelerated by the voltage, the capacitance energy (W) is transferred into kinetic energy. The reduction of capacitance energy also results in a decrease in the local bias U_{loc}, which in turn lowers the saturation velocity $v_s \propto U_{loc}$.[65,104–106] The charge velocity is therefore larger than the saturation velocity which results in strong electron scattering and limits the photocurrent. Furthermore, the carrier lifetime in the semiconductor substrate limits the length of the current pulse. The precise calculation of both effects[65] is beyond the scope of this work, but if the materials and the geometry are chosen correctly, sub-picosecond current pulses $I_{PC}(t)$ are produced in the PCA which then emit THz radiation.

The THz emission can be described as dipole radiation. The strong angular dependence of this radiation results in a strongly divergent THz beam. Usually, this radiation is collimated directly after the generation using a silicon lens. The refractive index of silicon is very similar to that of the PCA substrate, hence there are minimal reflection losses. Additionally, silicon has a large refractive index in the THz spectral range ($n_{Si} \approx 3.42$[107]) and is fairly easy to machine, which allows for a compact and small lens that can be mounted directly on the PCA chip. It is important to stress that the lens must be aligned precisely at the center of the emitter with micrometer precision. This can either be done with micrometer-precision screws in the research lab itself or the lens can be glued onto the chip, which is frequently offered in commercial PCAs.

The most commonly used semiconductor for the emitter is gallium arsenide (GaAs), either semi-insulating GaAs (SI-GaAs) or low-temperature grown GaAs (LT-GaAs). A less common one is radiation damaged silicon on sapphire (r-SOS). The carrier mobility in r-SOS is rather low ($\mu \approx 1500\,\frac{\mathrm{cm}^2}{\mathrm{Vs}}$)[106] compared to GaAs ($\mu \approx 8500\,\frac{\mathrm{cm}^2}{\mathrm{Vs}}$).[106] Additionally, the carrier lifetime in r-SOS ($\tau \approx 600$ fs)[108] is longer than in LT-GaAs ($\tau \approx 100$ fs).[109] Therefore, LT-GaAs is currently the material of choice for commercial emitters.

A drawback of GaAs is that it exhibits optical phonons at 8.5 THz[106] and, therefore, high frequency THz radiation is absorbed by the emitter before it can be routed to the spectrometer. This issue can be circumvented by using a thin GaAs layer of 1–2 µm. However, this material is too fragile for practical applications and performing lithography on it is impossible. Therefore, this thin layer of LT-GaAs must be bonded to a back-substrate such as silicon, which has a similar refractive index and is THz transparent. THz pulses of up to 10 THz bandwidth have been demonstrated with this technique.[101,103]

IV. THz DETECTION

Similar to THz generation, there are several different approaches for THz detection. For THz-TDS, only coherent detection mechanisms are suitable, and we will not consider thermal detectors such as bolometers and Golay cells.

As was the case for THz generation, we will present an overview of different techniques and then discuss detection via PCAs in detail.

A. THz detection overview

After a broadband THz pulse is generated, a detector with a greater or equal bandwidth is must be used to collect the spectral information. Most detectors do not exhibit a flat gain profile and the best signal-to-noise ratio (SNR) is obtained when the spectral gain of the detector and the emitter bandwidths are closely matched. Table II provides a brief overview over some detectors and some references for further study.

B. THz detection with PCAs

THz detection via photoconductive switches can be performed with similar or even identical devices as used for THz generation. In contrast to generation, the metal gap fabricated on the semiconductor is not externally biased. The electrical bias is created by the electrical field of the THz electromagnetic pulse. The laser beam focused on the semiconductor gap generates free carriers, which increases the conductivity of the device. Thus, a current is produced that is directly proportional to THz electric field.

The response function of the detector depends on the laser pulse length and the carrier lifetime. In contrast to the generation, where the stored energy also limits the current-pulse length, only the carrier lifetime is important in detection. Shorter carrier lifetimes result in a sharper temporal response, which in turn leads to larger THz bandwidths. The carrier lifetime in LT-GaAs is typically about 100 to 300 fs.

The THz-driven current is on the order of picoamperes to nanoamperes. Measuring such small currents is challenging in general and in particular because the thermal noise voltage (Johnson-Nyquist noise) is[121]

$$U_{noise} = \sqrt{\frac{k_B T}{C}}. \tag{8}$$

We can roughly approximate the capacitance to be $C \approx 10\,\text{fF}$.[65] The resulting noise voltage is then $U_{noise} \approx 650\,\mu\text{V}$. The dark resistance R of the antenna is in the order of 1 MΩ, resulting in a current noise of up to

$$I = U/R = 650\,\text{nA}. \tag{9}$$

Measuring a signal that is of the same order of magnitude as the noise requires selective amplification of the signal only.

TABLE II. Overview of some THz detectors. Acronyms used: ABCD, air-biased coherent detection; EOS, (free space) electro-optical sampling; PCA, photoconductive antenna; r-SOS, radiation damaged silicon-on-sapphire; LT-GaAs, low temperature grown gallium arsenide.

Detector name	Laser	Bandwidth (THz)	Reference
ABCD	Amplifier	0.1–120	87,110, and 111
EOS	Amp./Osci.		78 and 112–114
ZnTe		0.1–5	115–117
GaP		0.1–8	60 and 92
$LiNbO_3$		0.1–1	118–120
PCA	Oscillator		94
r-SOS		0.1–2	98 and 99
LT-GaAs		0.1–180	82,96, and 100–103

C. Lock-in detection

Lock-in amplifiers are used to measure small signals within a noisy background. A lock-in amplifier is a system that selectively amplifies a signal at a given reference frequency f. The noisy incoming signal is multiplied by a sine wave at the reference frequency and then sent through a low-pass filter to obtain the DC component, which is the signal of interest. The time constant of the low-pass filter is an extremely important parameter and is discussed below. For example, if a step function is passed through a low-pass filter, it will reach 95% of its final value after three time constants: $(1/e)^3$, and 99.3% after five time constants. Therefore, if one scans the delay line too fast, sharp features of the THz pulse will be broadened and attenuated. On the other hand, if one scans it too slow, there is no additional improvement.

The THz time-domain signal is modulated by switching the THz generation on and off at the desired reference frequency, which is referred to as "chopping." This can be achieved by applying a square wave bias voltage between 0 V and +10 V or by mechanically modulating the excitation beam with a chopper wheel.

In general, electronic modulation is preferred when using PCAs. Electronic switching allows for tens of kHz modulation frequencies that are significantly higher than mechanical modulation frequencies of 0.1 to 4 kHz. These higher chopper frequencies are desirable because thermal noise (pink noise or $1/f$ noise) is proportional to $1/f$, hence, higher lock-in frequencies result in lower noise. However, the highest usable modulation frequency is limited by the capacitance of the antenna as well as the frequency response of the cables, amplifiers, and other electronics. Therefore, it is recommended to empirically test which modulation frequency and method (mechanical vs. electronic) results in the best SNR.

V. PRACTICAL CONSIDERATIONS

In this section, we present suggestions for improving a THz-TDS system. However, we first define some figures-of-merit (FOMs) to benchmark a system. We will discuss all these FOMs by examples from the system used in our lab. For this section, the spectrometer was intentionally misaligned to provide substantial noise.

A. Characterizing the system: SNR and DNR

To estimate the usable bandwidth of the spectrometer, it is crucial to determine the SNR and the dynamic range (DNR). The noise floor is measured by placing a metal-block in the THz beam-path and measuring the *signal* using the same settings as during the actual measurement. The root-mean-square of the noise time trace is an excellent measure of the total noise. The amplitude of the time trace divided by this value is the first FOM for optimization. All frequency information of the THz pulse is contained in the time trace. For samples that are not strongly dispersive or absorbing, the amplitude of the time trace is a good approximation of the total THz power transmitted.

The Fourier transform of these measurements is used to determine the DNR, defined as ratio between signal intensity and noise intensity at a given frequency. In general, it is recommended to average both curves over a few GHz window to avoid spikes. These power spectra for our system are plotted in Fig. 4.

The maximum DNR at 0.9 THz is greater than 10^6 or 60 dB. At 2.5 THz, it is 25 dB. Therefore, measurements at frequencies below 2.5 THz are trustworthy. However, the user should keep in mind that the intensity DNR is only one of the two components of the complex-valued information from the measurement. Like the amplitude, the phase is also accompanied by noise. The origin of this noise is different. Amplitude noise is caused primarily by power fluctuations, while phase noise originates from temporal inaccuracy. Any imperfections in the delay line will increase the phase noise since the FFT assumes that the time-points are equally spaced.

To calculate the phase noise of a measurement, we perform the same measurement multiple times. The mean value of all iterations is defined as the baseline. The standard deviation of these iterations is a good approximation of the phase noise. The influence of the phase noise can be seen in Fig. 5, which shows the phase noise for the same measurement as in Fig. 4, and is surprisingly large.

While the intensity DNR at 2 THz is about 40 dB, the phase noise at the same frequency is ±20°. The influence of the uncertainty in phase directly manifests itself as uncertainty of the refractive index. The real part of the refractive index, n, of a loss-free sample is related to the phase change ($\Delta\phi$) by

$$\phi = n k_0 d, \tag{10}$$

$$n = \frac{\phi}{k_0 d}, \tag{11}$$

$$\Delta n = \frac{\Delta\phi}{k_0 d}, \tag{12}$$

where d is the thickness of the layer and k_0 the wavevector in vacuum. If we assume a silicon wafer with 550 µm thickness and a refractive index of 3.42,[107] the uncertainty in the THz range would result in 3.42 ± 0.03. However, a significantly thinner sample with smaller refractive index, for example, 5 µm of Nafion with refractive index of 1.58 at 1 THz[122] will lead to an extracted refractive index of 1.58 ± 3.33. This illustrates that minimizing the phase error is crucial for reliable extraction of refractive indices of thin layers. Several techniques to reduce the phase noise are discussed in Subsection V B.

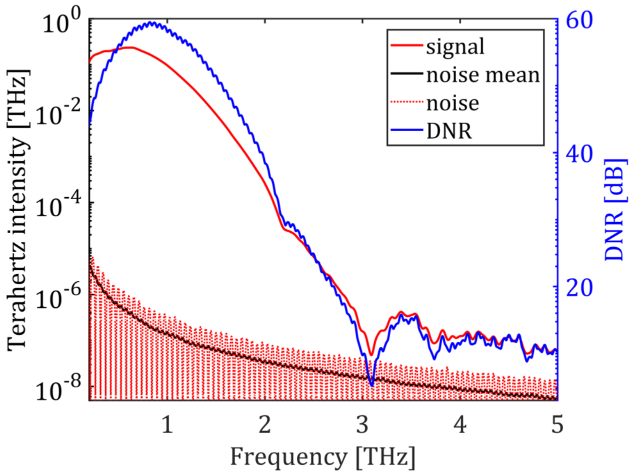

FIG. 4. Frequency-dependent intensity (red solid line) compared to the spectral intensity of a noise measurement (dotted red line). The black line is the noise smoothed with a 20 GHz frequency domain filter. The blue line is the dynamic range (DNR = signal/averaged noise).

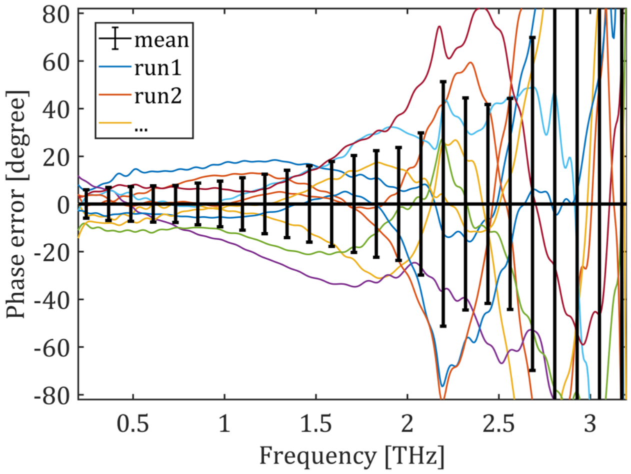

FIG. 5. Phase error averaged for ten measurements. The black bars depict the error, calculated as the standard deviation of the ten measurements. The colored lines are the individual traces. Compared to the previously shown DNR, the phase error is significant even for frequencies with high DNR, for example, at 2 THz.

B. Potential noise sources

After a rigorous characterization of the system, the best way to increase the SNR and DNR is by minimizing the noise, that is, it is typically easier to reduce noise rather than increase signal. There are many possible causes for noise in the system[123–125] and the remarks here are general in nature. We will not cover all potential noise sources for THz-TDS.

As stated previously, the ultrafast laser is at the heart of any THz-TDS system. Therefore, it is the largest source of noise. For example, if one completes his or her measurements for the day and returns the next morning to find that the noise has increased overnight, the best starting point for a noise investigation is the laser itself. Shot-to-shot fluctuations result in averaging over non-identical laser pulses. Since THz generation is usually nonlinear with respect to the laser power or pulse length, variations in laser intensity will, therefore, reduce the SNR due to a higher noise level. Furthermore, it is essential to ensure that the laser power is stable over the duration of a measurement, whether it is 5 min or 5 h.

Another source of noise is electrical noise. As discussed in Subsection IV C, the noise is typically lower for higher chopper frequencies (there are other types of noise, but 1/*f* noise dominates at the frequencies we use). However, there is a trade-off when the frequency response function of the antenna itself cannot support the high modulation frequency. Therefore, one must perform several SNR/DNR measurements with many different modulation frequencies to find the best one for the system. Naturally, one wants to avoid the AC line frequency and its harmonics, but there are often noise sources in the lab that are at different frequencies. Furthermore, it is possible that the bias voltage on the emitter somehow cross talks with the detector. Even minimal cross talk on the order of a femtoampere will result in a very high level of noise because the frequency of the cross talk is identical to the lock-in frequency. To track this down, it is advised to use a mechanical chopper to directly chop the THz beam instead of electrical modulation. This way, no electrical cross talk noise can occur. If the SNR is significantly better with mechanical chopping, the origin of the cross talk must be found.

As stated above, a particularly high phase noise is caused by temporal uncertainty. This can either be caused by the mechanical delay line, but air fluctuations and vibrations of the laser table are also potential culprits. To validate the performance of the delay stage, one should check the stability of beam pointing at a large distance. This can be done by eye, but more accurate results are achieved using a CCD camera to monitor the spot while moving the stage. This mechanical jitter can originate from the stage itself or from the optical mountings and posts on the stage. It is recommended to use highly stable full steel posts to avoid any bending or bouncing when moving the stage. If the jitter is not caused by the stage, air fluctuations need to be minimized.

Although it is tempting to evacuate the lab itself, this approach is unfeasible because it is difficult to adjust the optical mounts while wearing a space suit. Instead, any nitrogen inlets into the purge box should have a muffler to minimize both directional and turbulent air flow. In extreme cases, the optical beams must be enclosed in "light pipes" after the point of the beamsplitter.

The best technique to decrease the phase noise is to measure the difference signal between measurement and reference instead of making two separate measurements. This can be done by mounting the sample on a rapidly moving stage which brings it into and out of the beam path at tens to hundreds of Hz. This fast modulation can then be added to the chopper frequency, which allows the difference signal between sample and reference to be detected. This suppresses the noise and significantly increases the sensitivity.[126–128]

Even when all of these systematic sources of noise are identified and solved, noise will still remain in the system. Thus, there will always be scan-to-scan variability, which typically follows Gaussian statistics and will be proportional to $\frac{1}{\sqrt{N}}$, where N is the number of scans averaged together. The only way to reduce this noise is to increase N. In general, this increase can be accomplished either by measuring the full time trace multiple times (iterations) or by scanning slowly and integrating each time-point for a longer period of time. This integration is usually done at the lock-in amplifier by defining the time constant. As stated above, it is best to reduce the noise level itself to increase the SNR by that amount because signal averaging increases the SNR as a function of the square root of the time taken to make a measurement. For example, if the noise is reduced by a factor of five, then the SNR is increased by a factor of 5, but it would require an acquisition time of 25 times longer to achieve the same increase in SNR. Thus, if a typical scan takes 10 min to obtain, it will require 250 min (4 h 10 min) to increase the SNR by a factor of five. There are times when signal averaging is the only option, but one should strive to either increase the signal or decrease the noise before implementing it.

C. Time constant, scan speed, and scan length

The lock-in amplifier averages the signal over a period of time which is defined by the time constant (τ). This averaging has the advantage that some of the random noise is suppressed and the signal is smoother. If this were the only consideration, we would like this time constant to be as large as possible to give us the best SNR. However, while the delay stage is moving the signal is constantly changing because it is measuring different time-points of the THz signal. For example, in the case of a time constant of $\tau = 30$ ms and a high scan speed of 10 ps/s, every time-point is "averaged" with 0.9 to 1.5 ps of time-points after it (3 to 5 lock-in time constants).

It is important to choose the combination of lock-in time constant and scanning speed such that 3 to 5 time constants elapse in the time it takes the delay stage to move the distance corresponding to the sharpest feature in the THz pulse (and this could simply be a rising or falling edge rather than the actual pulse width). For example, if it is a typical value of 50 fs and the time constant is 30 ms, then 3 time constants will elapse over 50 fs of delay time when scanning at 0.55 ps/s, and five time constants will elapse when scanning at 0.33 ps/s.

The effect of the scan speed is illustrated in Fig. 6 by measuring the same pulse for the same total time, meaning that for faster scans more iterations were measured. The sampling rate was 128 Hz for a scan speed of $v = 0.5$ ps/s, and 512 Hz for $v = 5$ ps/s and $v = 10$ ps/s, all with a 30 ms lock-in time constant.

The magnitude of the signal is greatly reduced when scanning too fast. More importantly, the pulse changes shape and becomes much longer in the time-domain due to the low pass filter properties of the combination of lock-in time constant and scanning speed. As seen in Fig. 7, the corresponding frequency bandwidth is much smaller when scanning the delay line faster. The effect of this low pass filter is mathematically a convolution of the THz time-domain signal with a Gaussian function with time constant of $\sigma = \tau v$. The Fourier transform of a convolution of two functions is the product of the Fourier transformed functions[73]

$$F(t) \circledast \frac{1}{\sigma} e^{-\frac{t^2}{2\sigma^2}} \quad \xrightarrow{\text{FT}} \quad f(\omega) e^{-\frac{1}{2}\omega^2\sigma^2}. \tag{13}$$

Therefore, the THz spectra that would have been obtained with an infinitely short time constant are multiplied

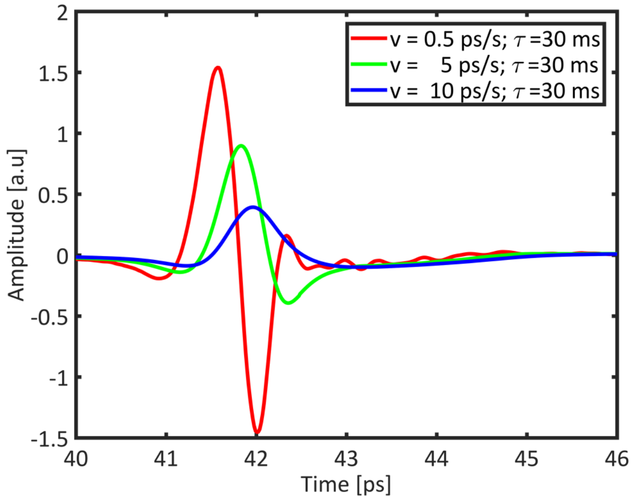

FIG. 6. Time trace of the same THz pulse using different scan speeds v. For comparison, the same total measurement time was used.

by a Gaussian window, centered around 0 THz, with a width of $1/\sigma$. This windowing suppresses higher frequencies and, therefore, reduces the DNR. The Fourier transforms of the time traces in Fig. 6 are plotted in Fig. 7. The three spectra are normalized to the noise floor and were measured using the same total measurement time.

In addition to the scan speed and integration time constant, the total time range (in ps) must be considered. Technically, the THz pulse is infinitely long, however, its amplitude decays rapidly as a function of time. This decay time depends on the spectral characteristics of the sample and the THz pulse. Without significant dispersion or absorption, the spectral information in the first few picoseconds of the THz signal provides all of the information that is needed. However, if the sample material is strongly dispersive or shows a sharp absorption feature a longer scan is required.

The influence of a narrow time window can also be understood with Fourier transforms. If we assume a Gaussian shaped absorption feature in the frequency domain, the resulting time-domain information is described by

$$f(\omega)=\frac{1}{\sigma}e^{-\frac{1}{2}\omega^2/\sigma^2} \quad \xrightarrow{\text{FT}} \quad e^{-\frac{1}{2}t^2\sigma^2}=F(t). \tag{14}$$

We see that a narrow frequency feature with width $\sigma=\frac{FWHM}{2\sqrt{2\ln 2}}$ will correspond to a time-domain trace that has features that persist for a long time ($\propto 1/\sigma$).

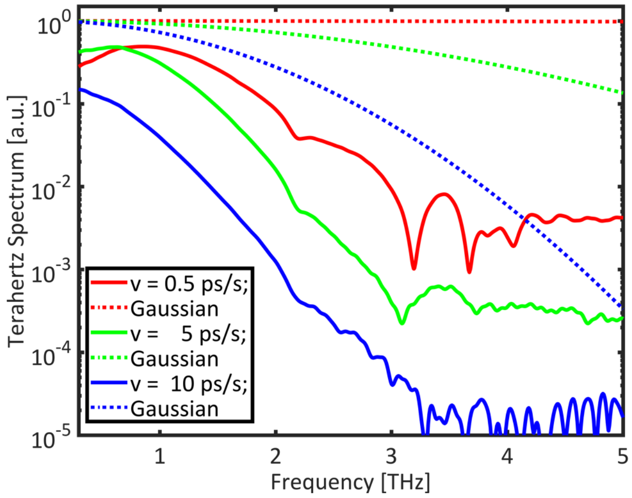

FIG. 7. THz spectra of the same pulse measured with the same time constant $\tau = 30$ ms at different scan speeds v. The dashed line is the calculated Fourier frequency filter for the time-domain convolution.

The influence of a short time window is illustrated by the simulated spectrum of a metamaterial absorber, as shown in Fig. 8. The full 88 ps time trace of this simulation is Fourier transformed and plotted as black line in the graph which is obscured by the other lines. The FWHM of the resonance is 23 GHz. The same time trace was then truncated after 30, 20, and 10 ps. The resulting Fourier transforms are plotted in red, blue, and green, respectively. The 10 ps time trace has distinct ringing. Furthermore, the FWHM of the *measured* resonance broadens to 65 GHz and is slightly red shifted. The direction and strength of the shift depends on the experimental conditions. In this case, the shift is caused by the unequal distribution of the frequency components in experimental time traces.

The broadening and ringing due to time truncation can also be understood based on the properties of Fourier transforms. Truncation in time domain is mathematically described as a multiplication with a Heaviside step-function $\Theta(t)$ going from 1 to 0 at the point of truncation. As a result, the Fourier transformation is described by

$$F(t)\Theta(t) \quad \xrightarrow{\text{FT}} \quad f(\omega)\circledast\mathcal{F}[\Theta(t)], \tag{15}$$

where $F(t)$ is the unconstrained THz signal and $\mathcal{F}[\Theta(t)]$ is the Fourier transform of the step function.

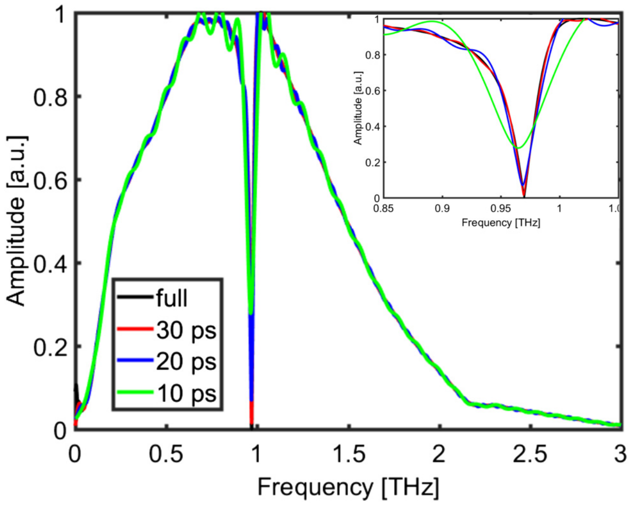

FIG. 8. Simulated THz spectra of an ideal electrical inductive-capacitive (ELC) metamaterial. The data were truncated in the time domain after 10, 20, or 30 ps. For comparison, the black line shows the results for the full data set of 88 ps. Truncation results in frequency broadening and ringing. The broadening and shifting is illustrated in the inset, which zooms in to the 0.85 to 1.05 THz frequency range. It is seen that truncation at 30 ps is essentially identical to the full time trace. There are slight distortions when truncating at 20 ps, and very large distortions when truncating at 10 ps.

The Fourier transform of a rectangular-function starting at t_1 (the beginning of the measurement) and ending at t_2 is[129]

$$\mathcal{F}[\Theta(t)] = \sqrt{\frac{\pi}{2}}\frac{\mathrm{i}}{2\omega}\left(e^{\mathrm{i}t_1\omega} - e^{\mathrm{i}t_2\omega}\right). \tag{16}$$

This function has the well-known intensity profile of the single slit diffraction experiment,[130] showing a center maximum and several minor side maxima. The width of the center maximum causes the resonance to broaden, while the side maxima create the ringing in the spectrum. Using Eqs. (16) and (15), the reader can estimate the resulting resolution of the THz-TDS system. Depending on the desired resolution, a suitable measurement time window can be chosen. Note that this resolution is not the same as the frequency step size based on the length of the time-domain signal (Δf = 1/T, where T is the total scan time).

In some cases, it is unavoidable to use a short time window to reduce the measurement time or to avoid reflections due to etalon effects. In the case of features due to etaloning, it is possible to not simply halt the data acquisition before the reflection feature appears, but rather to multiply the time traces with a Gaussian time window, centered around the temporal maximum of the THz-signal. The Fourier transform of a Gaussian window is again a Gaussian function, which will still broaden the spectral resonance, but not induce any ringing as is described above when a rectangular windowing function is used.

VI. APPLICATIONS OF THZ-TDS

THz-TDS has been used to study molecules in the gas phase,[131–134] liquids and solutions,[10,11,135,136] and the solid state.[2,14,19–21,23–27,137–140] The goal of all of these applications is to measure the frequency-dependent complex refractive index of the sample. In some experiments, the user is more interested in the imaginary part of the refractive index (i.e., resonant absorption and conductivity). In other cases, the real part is more interesting (e.g., layer thickness measurements). A significant advantage of THz-TDS is that the real and imaginary part of the refractive index are measured simultaneously. While it is true that these two are related through the Kramers-Kronig relationship, spectral information of frequencies from DC to infinity is required. There are many optical techniques in which the Kramers-Kronig relation or other models are used, but the limitation of $0 < \omega < \infty$ is always present.

We will illustrate how the refractive index of a sample can be calculated from experimental data. This illustration will start with the most general case and then present simplifications utilized with common experimental conditions. These examples are presented with a solid material as sample in mind, but they are easily generalized for liquids and gases.

A. General form of THz transfer function

The complex refractive index is calculated from the ratio of the complex transfer function of a sample and that for a reference.[130] The reference is shown in the top of the figure, and consists of the substrate (n_1, d_1), but not the layer of interest. The sample is a layer on top of this substrate resulting in a system of two layers as illustrated in the bottom of Fig. 9 with refractive indices n_1 and n_2 and thicknesses d_1 and d_2, with an interface with air (n_0) and a second known medium n_3, which is typically air. The transfer function for the sample is given by

$$E_\mathrm{s} = t_{01}P_1t_{12}P_2t_{23}FP_{012}FP_{123}E_\mathrm{i}, \tag{17}$$

where E_i is the input electric field. The complex transmission and reflection Fresnel coefficients, t_{jk} and r_{jk}, are[141]

$$t_{jk} = \frac{2n_j}{n_j + n_k} \qquad r_{jk} = \frac{n_j - n_k}{n_j + n_k}. \tag{18}$$

The propagation through layer j is[141]

$$P_j = \mathrm{e}^{-\mathrm{i}k_0 d_j n_j}, \tag{19}$$

where the wave vector in vacuum is $k_0 = \omega/c$. The Fabry-Pérot etalon caused by partial reflections of M pulse traces is given by

$$FP_{jkl} = \sum_{m=0}^{M}\left(r_{kl}P_kr_{jk}P_k\right)^m, \tag{20}$$

where M is the number of internal reflections measured and depends on the time separation between the reflections as well as the length of the THz-TDS signal time trace.

These equations are identical to the results achieved by setting up an ABCD matrix[130] and calculating the transfer function. However, the ABCD matrix method is only valid if *all* reflections are measured and is hence less suited for THz-TDS, since one typically does not measure all reflections for thick layers.

In addition to the transmission through the sample, a reference scan without sample present must also be taken to ensure that the result is independent of the THz spectrometer being used. In the case of a thick substrate, such as a pressed pellet, referencing can be accomplished with a simple air

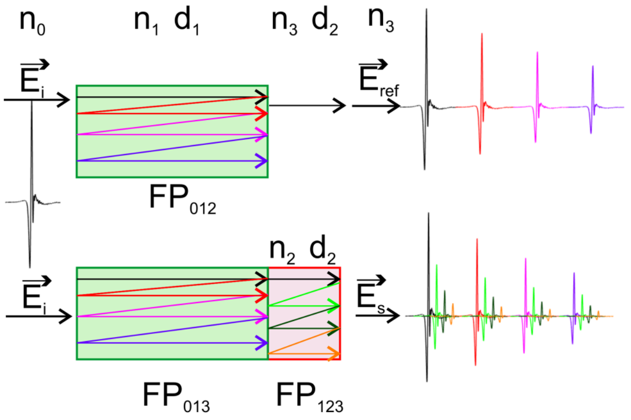

FIG. 9. Simplified representation for THz transmission through two layer system, with substrate refractive index n_1 and thickness d_1 and sample refractive index n_2 and thickness d_2. The system is embedded in air on the left side (n_0) and an infinitely large known material n_3 to the right, which is typically air and $n_3 = n_0$. The colored lines illustrate partially reflected signals. These lines are offset for clarity in reality they will fall in the same position as the main pulse. The multiple reflections M induce the Fabry-Pérot etalon FP$_{jkl}$.

measurement with no sample present. However, in the case of layered materials with a sample on a substrate, it is better to use transmission through the substrate alone without the sample material as a reference. The advantage of this referencing method is that the influence of the substrate thickness cancels out, and the coefficients P_1 and t_{01} are not needed in the final calculations.

The reference electric field transmitted though the substrate layer only is described by

$$E_{\mathrm{ref}} = t_{01}P_1 t_{13} P_3 FP_{013} E_{\mathrm{i}}. \tag{21}$$

Combining Eqs. (17) and (21), we have

$$\frac{E_{\mathrm{s}}}{E_{\mathrm{ref}}} = \frac{t_{01}P_1 t_{12} P_2 t_{23} FP_{012} FP_{123}}{t_{01} P_1 t_{13} P_3 FP_{013}}, \tag{22}$$

which simplifies to

$$\frac{E_{\mathrm{s}}}{E_{\mathrm{ref}}} = \frac{t_{12}t_{23}}{t_{13}} \frac{P_2}{P_3} \frac{FP_{012}FP_{123}}{FP_{013}}. \tag{23}$$

This relates the two experimentally measured THz fields to the unknown refractive index n_2 if all other refractive indices and all thicknesses are known. This equation can be solved numerically,[142,143] but it is possible to simplify this equation in most cases, as seen below.

B. Thick substrate

A common case is a thick substrate layer with an additional thick or thin sample layer. The m-th reflected pulse in the substrate [Eq. (20)] is delayed by $\Delta t = 2mn_1 d_1/c$. For a common substrate like a silicon wafer ($d_1 \approx 500\,\mu\mathrm{m}$, $n_1 \approx 3.42$)[107] or fused quartz ($d_1 \approx 1000\,\mu\mathrm{m}$, $n_1 \approx 2$),[107] this time delay is $\Delta t \approx 11$ ps for Si and $\Delta t \approx 13.2$ ps for $\mathrm{SiO_2}$. If we do not expect any sharp resonances in the sample material, we can truncate the time-domain signal prior to the first internal reflection in the substrate. The Fabry-Pérot etalon for $M = 0$ reflections simplifies to $FP_{012} = FP_{013} = 1$. Therefore, the equation that must be solved is

$$\frac{E_{\mathrm{s}}}{E_{\mathrm{ref}}} = \frac{t_{12}t_{23}}{t_{13}} \frac{P_2}{P_3} FP_{123}. \tag{24}$$

C. Thick substrate and thick sample

In the case that the sample material is also thick, the reflections in material 2 are also truncated ($FP_{123} = 1$), and Eq. (24) simplifies to

$$\frac{E_{\mathrm{s}}}{E_{\mathrm{ref}}} = \frac{t_{12}t_{23}}{t_{13}} \frac{P_2}{P_3}. \tag{25}$$

While this might appear to be a rather uncommon case, it is formally the same as measuring a thick sample material without substrate, where we simply describe the surrounding air as thick substrate. This is often accomplished by diluting the actual sample material in a host material with low THz absorption, such as Teflon.[144,145] This technique is commonly used to study amino acid crystals,[20,23] explosives,[29,146] and other absorbing materials.

$$\frac{E_{\mathrm{s}}}{E_{\mathrm{ref}}} = \frac{t_{12}^2}{1} \mathrm{e}^{-\mathrm{i}k_0 d_2 (n_2 - 1)}. \tag{26}$$

D. Thick substrate and thin sample

In the case of a thin sample, Eq. (24) can again be simplified. *Thin* indicates that all internal reflections are included in the measurement. Equation (20) describing the Fabry-Pérot reflections becomes an infinite sum and simplifies to[129]

$$FP_{jkl} = \sum_{m=0}^{M=\infty} (r_{kl}P_k r_{jk} P_k)^m = \frac{1}{1 + r_{jk} r_{kl} P_k^2}. \tag{27}$$

The resulting thin layer equation is given by

$$\frac{E_{\mathrm{s}}}{E_{\mathrm{ref}}} = \frac{t_{12}P_2 t_{23}}{t_{13}P_3} \frac{1}{1 + r_{23}r_{21}P_2^2}. \tag{28}$$

This equation can be solved numerically.[142,143] Additionally, we can assume that the real and imaginary components of $n_2(\nu)$ vary smoothly as a function of frequency. This significantly reduces the number of free parameters from two per frequency point (for example, 2048 parameters are required for a scan of 1024 frequency points) to 3-10 in total, depending on the model, and this dramatically increases the numerical stability.

There is a large range of possible models, including Drude[76] and Drude-Smith[147,148] for conducting materials, the Debye-Model[10,136,149] for lossy materials and liquids, and loss free models such as Sellmeier[150] and Cauchy[151]. All these models have different assumptions and validation ranges, therefore, choosing one should be done with care.

E. Thick substrate and thin highly conducting sample

The final case is a conductor as the thin sample material, for example, gold,[126] superconductor,[38] or a photoexcited layer.[147] In this case, the optical properties of the sample are dominated by the conductivity in the sample. The change in phase and the absorption in the sample layer must be negligibly small

$$\mathrm{Re}(n_2)k_0 d_2 \ll 1 \quad \text{and} \quad \mathrm{Im}(n_2)k_0 d_2 \ll 1. \tag{29}$$

A non-trivial Taylor expansion of Eq. (24) yields the Tinkham formula[34,126,152]

$$T = \frac{1 + n_1}{1 + n_1 Z_0 \sigma_2 d_2}, \tag{30}$$

where $T = E_s(\omega)/E_{ref}(\omega)$, $Z_0 = \sqrt{\frac{\mu_0}{\epsilon_0}} = 376.730\,\Omega$ is the impedance of free space, and σ_2 is the complex sheet conductivity of the sample material.

As for any approximation, Equation (29) needs to be validated for the film thicknesses and materials used. While this formula works for several systems,[34,38,126,152] it can also fail for seemingly similar experiments.[140,153]

F. Strongly absorbing powder samples

Determining the frequency-dependent absorption coefficient and refractive index of organic crystals such as amino acids, explosives, or drugs can be challenging. For example, amino acids are commonly received as polycrystalline powder. The powder itself is strongly scattering which significantly attenuates the transmitted THz signal. Furthermore, the absorption at the resonance frequency can reach values in the order of 500 cm^{-1}. The layer fabricated from this material must be homogeneous and less than 50 μm thick to allow at least 10% transmission. Such a thin layer is challenging to handle and determining its thickness is even more challenging.

One common solution to this problem is to mix the sample material with a transparent host material such as Teflon.[20] A mixture of 25 mg sample in 1000 mg Teflon results in a 3-4 mm thick pellet with a refractive index close to the refractive index of Teflon (n = 1.5).[20] The internal reflection from the sample is delayed by $\Delta t = 2d_2n_2/c = 37$ ps, so we can ignore any Fabry-Pérot terms which simplifies the calculation to that presented in Sec. VI C. For a pellet sample in air ($n_1 = 1$), the resulting equation is

$$\frac{E_s}{E_{ref}} = t_{12}t_{21}\frac{P_2}{P_1}. \tag{31}$$

Diluting the sample material in a non-absorbing host provides another important advantage. The resulting pellet will have a low overall absorption, meaning the refractive index will have a large real part [$\mathrm{Re}(n_2) \approx n_{\mathrm{Teflon}} = 1.5$] relative to the imaginary part [$\mathrm{Im}(n_2) \leq 0.025$]. This is important because the phase change $\Delta\phi$ due to propagation through the medium $\Delta\phi_{\mathrm{bulk}}(\nu = 1\mathrm{THz}) = \mathrm{Re}(n_2)k_0d_2 = 5760°$ is much larger than the phase change from the air-sample interfaces, defined by the complex Fresnel coefficients ($\Delta\phi_{\mathrm{interface}} \approx 1°$).[20] In the case of a highly diluted material, we can therefore ignore the phase change at the interfaces, hence approximating the Fresnel coefficient as real, and Eq. (31) can be separated into one term that describes the phase[20]

$$\phi\left(\frac{E_s}{E_{ref}}\right) \approx \phi\left(\frac{P_2}{P_1}\right) = \phi\left(\frac{e^{-ik_0d_2\mathrm{Re}(n_2)}}{e^{-ik_0d_21}}\right) \\ = -\mathrm{Re}[(n_2-1)k_0d_2] \tag{32}$$

and one that describes the amplitude[20]

$$A\left(\frac{E_s}{E_{ref}}\right) \approx \mathrm{Re}\left[\left(\frac{t_{12}t_{23}}{t_{13}}\right)A\left(\frac{P_2}{P_3}\right)\right] \\ = \mathrm{Re}[(t_{12}t_{21})(e^{-k_0d_2\mathrm{Im}(n_2)})]. \tag{33}$$

These equations can be solved analytically. The calculated refractive index $n_2 = n_{\mathrm{sample}}$ is that for the mixed pellet. The values for the pure sample material can be calculated from this result using an effective medium theory (EMT).[154–156]

G. Example data workup for strongly absorbing powder sample

As an example, we explicitly demonstrate this procedure when measuring the spectrum of a polycrystalline molecular crystal (DL-norleucine) mixed with Teflon. THz-TDS is not only sensitive to the molecule itself but also to the crystal lattice of the material. Therefore, it is possible to identify the conformation, or polymorph, of a molecular crystal. These conformations are often temperature-dependent and, therefore, these experiments are performed in a cryostat in which the sample temperature is accurately controlled.

A mixed pellet containing the amino acids DL-norleucine in Teflon is mounted in the cryostat and cooled to 100 K. The THz-transient through this sample is measured and the results are plotted in part (a) of Fig. 10. Fig. 10 shows a reference pulse through air (black), a sample pulse though pure Teflon (blue) and a sample pulse through a Teflon pellet with DL-norleucine (red), at a temperature of 100 K. The time traces exhibit reflections at 22.5 (reference) and 27 ps (pellet), which are caused by the THz-detector. These reflections are suppressed by multiplying the time trace with a Gaussian window. The time traces are then Fourier-transformed, and Eqs. (33) and (32) are used to calculate the real and imaginary components of the complex frequency-dependent refractive indices, as is plotted in part (b) of Fig. 10. Note the correlation between real and imaginary part, a change in the real part (dispersion) results in a local maximum in the imaginary part (absorption) of the refractive index. The experimental results fulfill the Kramers-Kronig relation by definition, but are calculated without using Kramers-Kronig.

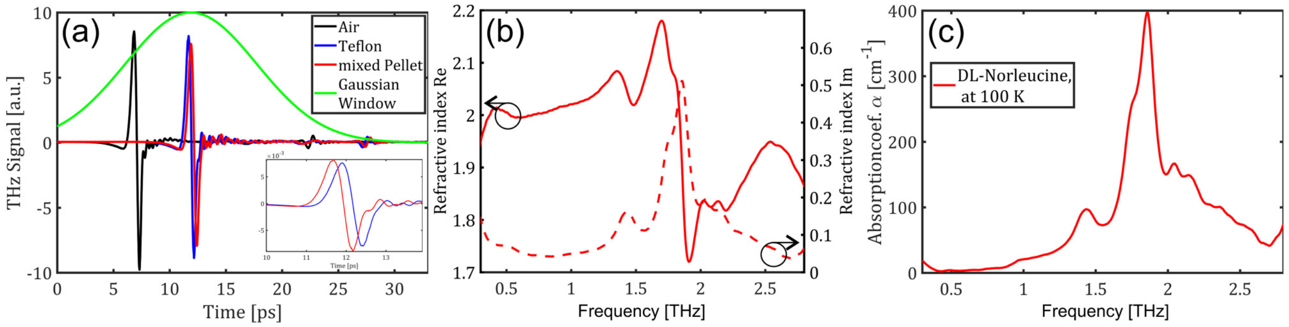

FIG. 10. Example for calculating absorption coefficients from measurements. An amino acid (DL-norleucine) is mixed with Teflon and pressed in a pellet. (a) Measured THz-time traces, a Gaussian window is used to suppress reflections. Inset: zoom on 10 to 13.5 ps, illustrating the temporal shift caused by the amino acid. (b) Refractive index of the pure pellet and the mixed pellet, both calculated using Eqs. (33) and (32). (c) Absorption coefficient of the pure sample materials, calculated from the refractive index using an effective medium theory.

The refractive index of pure Teflon [$\mathrm{Re}(n) \approx 1.5$, and $\mathrm{Im}(n) \approx 0$] is then used in an effective medium theory[154–156] to determine the complex refractive index of pure DL-norleucine. From the refractive index, we calculate the absorption coefficient as

$$\alpha = 2\ \mathrm{Im}(n)\frac{\omega}{c}. \tag{34}$$

The coefficient is plotted in part (c) of Fig. 10.

VII. CONCLUSION

Terahertz time-domain spectroscopy (THz-TDS) is a valuable technique in the fields of chemistry, physics, electrical engineering, materials science, and medicine. This tutorial has presented the basic concepts and terminologies to someone without any prior experience. The core principle of THz-TDS is that the electric field is measured in the time-domain.

By adjusting the relative distance that two ultrafast laser pulses travel, their timing is changed and the THz field can be sampled with femtosecond resolution. The Fourier transform of these time traces yields the spectral information. We showed that scans with delay times that are too short results in spectral broadening of absorption features, and a scanning speed that is too high causes a reduction of the THz bandwidth.

A significant advantage of THz-TDS is that the THz spectrum is complex-valued, meaning it provides amplitude and phase information at every frequency point within the usable bandwidth. This information can be used to directly calculate the complex refractive index of a sample without the need of the Kramers-Kronig analysis or empirical models. This advantage was demonstrated with general examples, and then in more detail for mixed samples consisting of strongly absorbing materials diluted in a transparent host. The used matlab scripts can be downloaded free of charge from https://thz.yale.edu.

ACKNOWLEDGMENTS

The authors acknowledge financial support by the National Science Foundation under Grant No. NSF CHE—CSDMA 1465085. We would like to thank Jacob Spies, Sarah Ostresh, Korina Straube, and Golo Storch for proof reading the manuscript and helpful suggestions.

[1] B. Fischer, M. Hoffmann, H. Helm, G. Modjesch, and P. U. Jepsen, Semicond. Sci. Technol. **20**, S246 (2005).
[2] M. Hangyo, M. Tani, and T. Nagashima, Int. J. Infrared Millimeter Waves **26**, 1661 (2005).
[3] T. Kleine-Ostmann and T. Nagatsuma, J. Infrared Millimeter Terahertz Waves **32**, 143 (2011).
[4] E. P. J. Parrott, Y. Sun, and E. Pickwell-MacPherson, J. Mol. Struct. **1006**, 66 (2011).
[5] A. J. Zeitler, T. F. Philip, A. Newnham David, M. Pepper, G. C. Keith, and T. Rades, J. Pharm. Pharmacol. **59**, 209 (2007).
[6] It is important to make the distinction between THz-TDS and THz Time Resolved Spectroscopy (TRTS). TRTS is a transient absorption technique in which changes in the THz spectrum are monitored after photoexcitation of the sample or some other means of changing its properties. THz-TDS probes materials that are in equilibrium and is similar to a Fourier transform infrared (FTIR) instrument, with the key difference that both the refractive index and absorption coefficient are obtained without invoking a Kramers-Kronig transform.
[7] S. S. Dhillon, M. S. Vitiello, E. H. Linfield, A. G. Davies, M. C. Hoffmann, J. Booske, C. Paoloni, M. Gensch, P. Weightman, G. P. Williams, E. Castro-Camus, D. R. S. Cumming, F. Simoens, I. Escorcia-Carranza, J. Grant, S. Lucyszyn, M. Kuwata-Gonokami, K. Konishi, M. Koch, C. A. Schmuttenmaer, T. L. Cocker, R. Huber, A. G. Markelz, Z. D. Taylor, V. P. Wallace, J. A. Zeitler, J. Sibik, T. M. Korter, B. Ellison, S. Rea, P. Goldsmith, K. B. Cooper, R. Appleby, D. Pardo, P. G. Huggard, V. Krozer, H. Shams, M. Fice, C. Renaud, A. Seeds, A. Stöhr, M. Naftaly, N. Ridler, R. Clarke, J. E. Cunningham, and M. B. Johnston, J. Phys. D Appl. Phys. **50**, 043001 (2017).
[8] M. Tonouchi, Nat. Photon **1**, 97 (2007).
[9] P. U. Jepsen, D. G. Cooke, and M. Koch, Laser Photonics Rev. **5**, 124 (2011).
[10] J. T. Kindt and C. A. Schmuttenmaer, J. Phys. Chem. **100**, 10373 (1996).
[11] B. Reinhard, K. M. Schmitt, V. Wollrab, J. Neu, R. Beigang, and M. Rahm, Appl. Phys. Lett. **100**, 221101 (2012).
[12] R. M. Dreizler and E. K. U. Gross, *Density Functional Theory an Approach to the Quantum Many-Body Problem* (Springer, 1990).
[13] M. Orio, D. A. Pantazis, and F. Neese, Photosynth. Res. **102**, 443 (2009).
[14] T. M. Korter, R. Balu, M. B. Campbell, M. C. Beard, S. K. Gregurick, and E. J. Heilweil, Chem. Phys. Lett. **418**, 65 (2006).
[15] D. G. Allis, A. M. Fedor, T. M. Korter, J. E. Bjarnason, and E. R. Brown, Chem. Phys. Lett. **440**, 203 (2007).
[16] M. D. King, W. D. Buchanan, and T. M. Korter, Anal. Chem. **83**, 3786 (2011).
[17] D. G. Allis, D. A. Prokhorova, and T. M. Korter, J. Phys. Chem. A **110**, 1951 (2006).
[18] M. D. King, P. M. Hakey, and T. M. Korter, J. Phys. Chem. A **114**, 2945 (2010).
[19] B. Yu, F. Zeng, Y. Yang, Q. Xing, A. Chechin, X. Xin, I. Zeylikovich, and R. R. Alfano, Biophys. J. **86**, 1649 (2004).
[20] J. Neu, C. T. Nemes, K. P. Regan, M. R. Williams, and C. A. Schmuttenmaer, Phys. Chem. Chem. Phys. **20**, 276 (2018).
[21] J. Neu, H. Nikonow, and C. A. Schmuttenmaer, J. Phys. Chem. A **122**, 5978–5982 (2018).
[22] M. R. C. Williams, A. B. True, A. F. Izmaylov, T. A. French, K. Schroeck, and C. A. Schmuttenmaer, Phys. Chem. Chem. Phys. **13**, 11719 (2011).
[23] M. R. C. Williams, D. J. Aschaffenburg, B. K. Ofori-Okai, and C. A. Schmuttenmaer, J. Phys. Chem. B **117**, 10444 (2013).
[24] M. Yamaguchi, K. Yamamoto, M. Tani, and M. Hangyo, in *2005 Joint 30th International Conference on Infrared and Millimeter Waves and 13th International Conference on Terahertz Electronics* (IEEE, 2005), Vol. 2, pp. 477–478.
[25] M. Yamaguchi, K. Yamamoto, M. Tani, and M. Hangyo, in *Infrared and Millimeter Waves, Conference Digest of the 2004 Joint 29th International Conference on 2004 and 12th International Conference on Terahertz Electronics, 2004* (IEEE, 2004), pp. 779–780.
[26] R. J. Falconer and A. G. Markelz, J. Infrared Millimeter Terahertz Waves **33**, 973 (2012).
[27] M. Lu, J. Shen, N. Li, Y. Zhang, C. Zhang, L. Liang, and X. Xu, J. Appl. Phys. **100**, 103104 (2006).
[28] Y. C. Shen, T. Lo, P. F. Taday, B. E. Cole, W. R. Tribe, and M. C. Kemp, Appl. Phys. Lett. **86**, 241116 (2005).
[29] M. R. Leahy-Hoppa, M. J. Fitch, X. Zheng, L. M. Hayden, and R. Osiander, Chem. Phys. Lett. **434**, 227 (2007).
[30] M. C. Kemp, in *2007 Joint 32nd International Conference on Infrared and Millimeter Waves and the 15th International Conference on Terahertz Electronics* (IEEE, 2007), pp. 647–648.
[31] F. Ellrich, G. Torosyan, S. Wohnsiedler, S. Bachtler, A. Hachimi, J. Jonuscheit, R. Beigang, F. Platte, K. Nalpantidis, T. Sprenger, and D. Hübsch, in *2012 37th International Conference on Infrared, Millimeter, and Terahertz Waves* (IEEE, 2012), pp. 1–2.
[32] J. F. Federici, B. Schulkin, F. Huang, D. Gary, R. Barat, F. Oliveira, and D. Zimdars, Semicond. Sci. Technol. **20**, S266 (2005).
[33] A. G. Davies, A. D. Burnett, W. Fan, E. H. Linfield, and J. E. Cunningham, Mater. Today **11**, 18 (2008).
[34] J. Lloyd-Hughes and T.-I. Jeon, J. Infrared Millimeter Terahertz Waves **33**, 871 (2012).
[35] R. Valdés Aguilar, A. V. Stier, W. Liu, L. S. Bilbro, D. K. George, N. Bansal, L. Wu, J. Cerne, A. G. Markelz, S. Oh, and N. P. Armitage, Phys. Rev. Lett. **108**, 087403 (2012).
[36] S. Sim, M. Brahlek, N. Koirala, S. Cha, S. Oh, and H. Choi, Phys. Rev. B **89**, 165137 (2014).
[37] R. Matsunaga, Y. I. Hamada, K. Makise, Y. Uzawa, H. Terai, Z. Wang, and R. Shimano, Phys. Rev. Lett. **111**, 057002 (2013).
[38] M. C. Nuss, K. W. Goossen, P. M. Mankiewich, and M. L. O'Malley, Appl. Phys. Lett. **58**, 2561 (1991).

[39] J. Li and K. Chang, Appl. Phys. Lett. **95**, 222110 (2009).
[40] R. Valdés Aguilar, A. V. Stier, W. Liu, L. S. Bilbro, D. K. George, N. Bansal, L. Wu, J. Cerne, A. G. Markelz, S. Oh, and N. P. Armitage, Phys. Rev. Lett. **108**, 087403 (2012).
[41] P. A. George, J. Strait, J. Dawlaty, S. Shivaraman, M. Chandrashekhar, F. Rana, and M. G. Spencer, Nano Lett. **8**, 4248 (2008).
[42] T. Otsuji, S. A. B. Tombet, A. Satou, H. Fukidome, M. Suemitsu, E. Sano, V. Popov, M. Ryzhii, and V. Ryzhii, J. Phys. D Appl. Phys. **45**, 303001 (2012).
[43] J. D. Buron, D. H. Petersen, P. Boggild, D. G. Cooke, M. Hilke, J. Sun, E. Whiteway, P. F. Nielsen, O. Hansen, A. Yurgens, and P. U. Jepsen, Nano Lett. **12**, 5074 (2012).
[44] T. Yasui, T. Yasuda, K.-i. Sawanaka, and T. Araki, Appl. Opt. **44**, 6849 (2005).
[45] K. Su, Y. C. Shen, and J. A. Zeitler, IEEE Trans. THz Sci. Technol. **4**, 432 (2014).
[46] S. Krimi, J. Klier, J. Jonuscheit, G. von Freymann, R. Urbansky, and R. Beigang, Appl. Phys. Lett. **109**, 021105 (2016).
[47] C. Yu, S. Fan, Y. Sun, and E. Pickwell-MacPherson, Quant. Imaging Med. Surg. **2**, 33 (2012).
[48] F. Shuting, B. S. Y. Ung, E. P. J. Parrott, V. P. Wallace, and E. Pickwell-MacPherson, J. Biophotonics **10**, 1143 (2016).
[49] S. J. Park, J. T. Hong, S. J. Choi, H. S. Kim, W. K. Park, S. T. Han, J. Y. Park, S. Lee, D. S. Kim, and Y. H. Ahn, Sci. Rep. **4**, 4988 (2014).
[50] A. Berrier, M. C. Schaafsma, G. Nonglaton, J. Bergquist, and J. G. Rivas, Biomed. Opt. Express **3**, 2937 (2012).
[51] S. J. Park, S. H. Cha, G. A. Shin, and Y. H. Ahn, Biomed. Opt. Express **8**, 3551 (2017).
[52] A. K. Sarychev and V. M. Shalaev, *Electrodynamics of Metamaterials* (World Scientific, 2007).
[53] T. J. Cui, D. R. Smith, and R. Liu, *Metamaterials, Theory, Design and Applications* (Springer, 2010).
[54] O. Paul, R. Beigang, and M. Rahm, Opt. Express **17**, 18590 (2009).
[55] Z. Wu, J. Kinast, M. E. Gehm, and H. Xin, Opt. Express **16**, 16442 (2008).
[56] M. A. Hoeh, J. Neu, K. Schmitt, and M. Rahm, Opt. Mater. Express **5**, 408 (2015).
[57] J. Neu, B. Krolla, O. Paul, B. Reinhard, R. Beigang, and M. Rahm, Opt. Express **18**, 27748 (2010).
[58] Y. Monnai, H. Shinoda, and H. Hillmer, Appl. Phys. B Lasers Opt. **103**, 1 (2011).
[59] J. Neu, R. Beigang, and M. Rahm, Appl. Phys. Lett. **103**, 041109 (2013).
[60] M. F. Volk, B. Reinhard, J. Neu, R. Beigang, and M. Rahm, Opt. Lett. **38**, 2156 (2013).
[61] N. I. Landy, S. Sajuyigbe, J. J. Mock, D. R. Smith, and W. J. Padilla, Phys. Rev. Lett. **100**, 207402 (2008).
[62] Sakai, Tani, Gu, Ohtake, Ono, Sarukura, Kadoya, Hirakawa, Matsura, Ito, Nishizawa, Hangyo, Nagashima, Wada, Torminaga, Oka, Kida, Tonouchi, Hermann, Fukasawa, and Morikawa, *Terahertz Optoelectronics*, edited by K. Sakai (Springer, 2005).
[63] S. Dexheimer, *Terahertz Spectroscopy: Principles and Applications, Optical Science and Engineering* (Taylor & Francis, 2007).
[64] Y.-S. Lee, *Principles of Terahertz Sciences and Technology* (Springer, 2009).
[65] P. U. Jepsen, R. H. Jacobsen, and S. R. Keiding, J. Opt. Soc. Am. B **13**, 2424 (1996).
[66] M. van Exter, C. Fattinger, and D. Grischkowsky, Opt. Lett. **14**, 1128 (1989).
[67] X. Xin, H. Altan, A. Saint, D. Matten, and R. R. Alfano, J. Appl. Phys. **100**, 094905 (2006).
[68] S. C. Howells and L. A. Schlie, Appl. Phys. Lett. **69**, 550 (1996).
[69] L. Thrane, R. H. Jacobsen, P. Uhd Jepsen, and S. R. Keiding, Chem. Phys. Lett. **240**, 330 (1995).
[70] H. Hirori, K. Yamashita, M. Nagai, and K. Tanaka, Jpn. J. Appl. Phys. **43**, L1287 (2004).
[71] A. Bitzer, H. Merbold, A. Thoman, T. Feurer, H. Helm, and M. Walther, Opt. Express **17**, 5 (2009).
[72] J. N. C. van der Valk and P. C. M. Planken, Appl. Phys. Lett. **81**, 1558 (2002).
[73] J. Mathews and R. L. Walker, *Mathematical Methods of Physics* (W.A. Benjamin, 1970).
[74] D. Sundararajan, *The Discrete Fourier Transform Theory, Algorithms and Applications* (World Scientific, 2001).
[75] J. S. Walker, *Fast Fourier Transforms* (CRC Press, 1996).
[76] J. D. Jackson, *Classical Electrodynamics*, 3rd ed. (John Wiley, 1999).
[77] K. Wynne and J. J. Carey, Opt. Commun. **256**, 400 (2005).
[78] A. Nahata, A. S. Weling, and T. F. Heinz, Appl. Phys. Lett. **69**, 2321 (1996).
[79] F. Blanchard, L. Razzari, H.-C. Bandulet, G. Sharma, R. Morandotti, J.-C. Kieffer, T. Ozaki, M. Reid, H. F. Tiedje, H. K. Haugen, and F. A. Hegmann, Opt. Express **15**, 13212 (2007).
[80] A. Schneider, M. Neis, M. Stillhart, B. Ruiz, R. U. A. Khan, and P. Günter, J. Opt. Soc. Am. B **23**, 1822 (2006).
[81] A. Schneider, I. Biaggio, and P. Günter, Opt. Commun. **224**, 337 (2003).
[82] I. Katayama, R. Akai, M. Bito, E. Matsubara, and M. Ashida, Opt. Express **21**, 16248 (2013).
[83] K.-L. Yeh, M. C. Hoffmann, J. Hebling, and K. A. Nelson, Appl. Phys. Lett. **90**, 171121 (2007).
[84] M. C. Hoffmann, K.-L. Yeh, J. Hebling, and K. A. Nelson, Opt. Express **15**, 11706 (2007).
[85] J. A. Fülöp, L. Palfalvi, G. Almasi, and J. Hebling, J. Infrared Millimeter Terahertz Waves **32**, 553 (2011).
[86] I. Babushkin, W. Kuehn, C. Köhler, S. Skupin, L. Bergé, K. Reimann, M. Woerner, J. Herrmann, and T. Elsaesser, Phys. Rev. Lett. **105**, 053903 (2010).
[87] E. Matsubara, M. Nagai, and M. Ashida, J. Opt. Soc. Am. B **30**, 1627 (2013).
[88] H. G. Roskos, M. D. Thomson, M. Kre, and T. Löffler, Laser Photon. Rev. **1**, 349 (2007).
[89] V. Apostolopoulos and M. E. Barnes, J. Phys. D Appl. Phys. **47**, 374002 (2014).
[90] G. Klatt, F. Hilser, W. Qiao, M. Beck, R. Gebs, A. Bartels, K. Huska, U. Lemmer, G. Bastian, M. B. Johnston, M. Fischer, J. Faist, and T. Dekorsy, Opt. Express **18**, 4939 (2010).
[91] G. Matthäus, T. Schreiber, J. Limpert, S. Nolte, G. Torosyan, R. Beigang, S. Riehemann, G. Notni, and A. Tünnermann, Opt. Commun. **261**, 114 (2006).
[92] T. Seifert, S. Jaiswal, U. Martens, J. Hannegan, L. Braun, P. Maldonado, F. Freimuth, A. Kronenberg, J. Henrizi, I. Radu, E. Beaurepaire, Y. Mokrousov, P. M. Oppeneer, M. Jourdan, G. Jakob, D. Turchinovich, L. M. Hayden, M. Wolf, M. Münzenberg, M. Kläui, and T. Kampfrath, Nat. Photonics **10**, 483 (2016).
[93] G. Torosyan, S. Keller, L. Scheuer, R. Beigang, and E. T. Papaioannou, Sci. Rep. **8**, 1311 (2018).
[94] N. M. Burford and M. O. El-Shenawee, Opt. Eng. **56**, 010901 (2017).
[95] L. Duvillaret, F. Garet, J. Roux, and J. Coutaz, IEEE J. Sel. Top. Quantum Electron. **7**, 615 (2001).
[96] M. Tani, S. Matsuura, K. Sakai, and S.-I. Nakashima, Appl. Opt. **36**, 7853 (1997).
[97] S. Winnerl, F. Peter, S. Nitsche, A. Dreyhaupt, B. Zimmermann, M. Wagner, H. Schneider, M. Helm, and K. Kohler, IEEE J. Sel. Top. Quantum Electron. **14**, 449 (2008).
[98] P. R. Smith, D. H. Auston, and M. C. Nuss, IEEE J. Quantum Electron. **24**, 255 (1988).
[99] M. van Exter and D. R. Grischkowsky, IEEE Trans. Microw. Theory Technol. **38**, 1684 (1990).
[100] Y. C. Shen, P. C. Upadhya, H. E. Beere, E. H. Linfield, A. G. Davies, I. S. Gregory, C. Baker, W. R. Tribe, and M. J. Evans, Appl. Phys. Lett. **85**, 164 (2004).
[101] M. Klos, R. Bartholdt, J. Klier, J. F. Lampin, and R. Beigang, in *2015 40th International Conference on Infrared, Millimeter, and Terahertz Waves (IRMMW-THz)* (IEEE, 2015).
[102] L. Desplanque, J. F. Lampin, and F. Mollot, Appl. Phys. Lett. **84**, 2049 (2004).
[103] H. Heiliger, M. Vossebürger, H. G. Roskos, H. Kurz, R. Hey, and K. Ploog, Appl. Phys. Lett. **69**, 2903 (1996).
[104] J.-H. Son, T. B. Norris, and J. F. Whitaker, J. Opt. Soc. Am. B **11**, 2519 (1994).
[105] J. E. Pedersen, V. G. Lyssenko, J. M. Hvam, P. U. Jepsen, S. R. Keiding, C. B. Sorensen, and P. E. Lindelof, Appl. Phys. Lett. **62**, 1265 (1993).
[106] S. Sze and K. Ng, *Physics of Semiconductor Devices* (John Wiley & Sons, 2006).
[107] D. Grischkowsky, S. Keiding, M. van Exter, and C. Fattinger, J. Opt. Soc. Am. B **7**, 2006 (1990).
[108] F. E. Doany, D. Grischkowsky, and C. Chi, Appl. Phys. Lett. **50**, 460 (1987).
[109] M. Stellmacher, J.-P. Schnell, D. Adam, and J. Nagle, Appl. Phys. Lett. **74**, 1239 (1999).
[110] I.-C. Ho, X. Guo, and X.-C. Zhang, Opt. Express **18**, 2872 (2010).

[111] T. Wang, K. Iwaszczuk, E. A. Wrisberg, E. V. Denning, and P. U. Jepsen, J. Infrared Millimeter Terahertz Waves **37**, 592 (2016).

[112] N. C. J. van der Valk, T. Wenckebach, and P. C. M. Planken, J. Opt. Soc. Am. B **21**, 622 (2004).

[113] Q. W. X. Zhang, Opt. Quantum Electron. **28**, 945 (1996).

[114] Q. Wu and X. Zhang, Appl. Phys. Lett. **67**, 3523 (1995).

[115] P. C. M. Planken, H.-K. Nienhuys, H. J. Bakker, and T. Wenckebach, J. Opt. Soc. Am. B **18**, 313 (2001).

[116] Q. Wu, M. Litz, and X. Zhang, Appl. Phys. Lett. **68**, 2924 (1996).

[117] J. Neu and M. Rahm, Opt. Express **23**, 12900 (2015).

[118] C. Winnewisser, P. U. Jepsen, M. Schall, V. Schyja, and H. Helm, Appl. Phys. Lett. **70**, 3069 (1997).

[119] Y. Wang, H. Ni, W. Zhan, J. Yuan, and R. Wang, Opt. Mater. **35**, 596 (2013).

[120] M. Tani, K. Horita, T. Kinoshita, C. T. Que, E. Estacio, K. Yamamoto, and M. I. Bakunov, Opt. Express **19**, 19901 (2011).

[121] R. C. Jaeger and T. N. Blalock, *Microelectronic Circuit Design* (McGrawHill, 2016).

[122] S. O. Yurchenko and K. I. Zaytsev, J. Appl. Phys. **116**, 113508 (2014).

[123] A. Rehn, D. Jahn, J. C. Balzer, and M. Koch, Opt. Express **25**, 6712 (2017).

[124] W. Withayachumnankul, B. M. Fischer, H. Lin, and D. Abbott, J. Opt. Soc. Am. B **25**, 1059 (2008).

[125] L. Duvillaret, F. Garet, and J.-L. Coutaz, J. Opt. Soc. Am. B **17**, 452 (2000).

[126] M. Walther, D. G. Cooke, C. Sherstan, M. Hajar, M. R. Freeman, and F. A. Hegmann, Phys. Rev. B **76**, 125408 (2007).

[127] K. Iwaszczuk, D. G. Cooke, M. Fujiwara, H. Hashimoto, and P. U. Jepsen, Opt. Express **17**, 21969 (2009).

[128] Z. Jiang, M. Li, and X.-C. Zhang, Appl. Phys. Lett. **76**, 3221 (2000).

[129] I. N. Bronstein, K. A. Semendjajew, G. Musiol, and H. Mühlig, *Handbook of Mathematics* (Springer, 2007).

[130] E. Hecht, *Optics* (de Gruyter, Berlin, 2014).

[131] D. M. Mittleman, R. H. Jacobsen, R. Neelamani, R. G. Baraniuk, and M. C. Nuss, Appl. Phys. B **67**, 379 (1998).

[132] H. Harde, N. Katzenellenbogen, and D. Grischkowsky, J. Opt. Soc. Am. B **11**, 1018 (1994).

[133] H. Harde and D. Grischkowsky, J. Opt. Soc. Am. B **8**, 1642 (1991).

[134] R. R. Jones, D. You, and P. H. Bucksbaum, Phys. Rev. Lett. **70**, 1236 (1993).

[135] L. Xie, Y. Yao, and Y. Ying, Appl. Spectrosc. Rev. **49**, 448 (2014).

[136] U. Møller, D. G. Cooke, K. Tanaka, and P. U. Jepsen, J. Opt. Soc. Am. B **26**, A113 (2009).

[137] J. Neu, D. J. Aschaffenburg, M. R. C. Williams, and C. A. Schmuttenmaer, IEEE Trans. THz Sci. Technol. **7**, 755 (2017).

[138] J.-L. Garcia-Pomar, B. Reinhard, J. Neu, V. Wollrab, O. Paul, R. Beigang, and M. Rahm, Proc. SPIE **7945**, 7 (2011).

[139] B. Reinhard, K. Schmitt, T. Fip, M. Volk, J. Neu, A.-K. Mahro, R. Beigang, and M. Rahm, Proc. SPIE **8585**, 11 (2013).

[140] K. P. Regan, J. R. Swierk, J. Neu, and C. A. Schmuttenmaer, J. Phys. Chem. C **121**, 15949 (2017).

[141] S. J. Orfanidis, *Electromagnetic Waves and Antennas* (Rutgers University, 2006).

[142] L. Duvillaret, F. Garet, and J. L. Coutaz, IEEE J. Sel. Top. Quantum Electron. **2**, 739 (1996).

[143] I. Pupeza, R. Wilk, and M. Koch, Opt. Express **15**, 4335 (2007).

[144] F. D'Angelo, Z. Mics, M. Bonn, and D. Turchinovich, Opt. Express **22**, 12475 (2014).

[145] P. D. Cunningham, N. N. Valdes, F. A. Vallejo, L. M. Hayden, B. Polishak, X.-H. Zhou, J. Luo, A. K.-Y. Jen, J. C. Williams, and R. J. Twieg, J. Appl. Phys. **109**, 043505 (2011).

[146] M. J. Fitch, M. R. Leahy-Hoppa, E. W. Ott, and R. Osiander, Chem. Phys. Lett. **443**, 284 (2007).

[147] M. C. Beard, G. M. Turner, and C. A. Schmuttenmaer, Phys. Rev. B **62**, 15764 (2000).

[148] G. M. Turner, M. C. Beard, and C. A. Schmuttenmaer, J. Phys. Chem. B **106**, 11716 (2002).

[149] H. J. Liebe, G. A. Hufford, and T. Manabe, Int. J. Infrared Millimeter Waves **12**, 659 (1991).

[150] W. von Sellmeier, Ann. Phys. **143**, 272 (1871).

[151] D. Y. Smith, M. Inokuti, and W. Karstens, J. Phys. Condens. Matter **13**, 3883 (2001).

[152] R. E. Glover and M. Tinkham, Phys. Rev. **108**, 243 (1957).

[153] J. Neu, K. Regan, J. R. Swierk, and C. A. Schmuttenmaer, Appl. Phys. Lett. **113**(22), 233901 (2018).

[154] V. A. Markel, J. Opt. Soc. Am. A **33**, 1244 (2016).

[155] T. Choy, *Effective Medium Theory: Principles and Applications* (Clarendon Press, 1999).

[156] M. T. Prinkey, A. Lakhtakia, and B. Shanker, Optik **96**, 25 (1994), available at https://pennstate.pure.elsevier.com/en/publications/on-the-extended-maxwell-garnett-and-the-extended-burggeman-approa.